International Journal of Mechanical Sciences 223 (2022) 107299

Contents lists available at ScienceDirect

International Journal of Mechanical Sciences

journal homepage: www.elsevier.com/locate/ijmecsci

Theoretical, numerical, and experimental studies of a frequency up-conversion piezoelectric energy harvester

Zhongjie Li [a,b,c], Xuzhang Peng [b], Guobiao Hu [d,*], Yan Peng [a]

[a] School of Artificial Intelligence, Shanghai University, Shanghai 200444, PR China
[b] School of Mechatronic Engineering and Automation, Shanghai University, Shanghai 200444, PR China
[c] Engineering Research Center of Unmanned Intelligent Marine Equipment, Shanghai University, Shanghai 200444, PR China
[d] School of Civil and Environmental Engineering, Nanyang Technological University, 50 Nanyang Avenue 639798, Singapore

ARTICLE INFO

Keywords:
Piezoelectric stack
Frequency up-conversion
Averaging method
Equivalent circuit model
Two-degree-of-freedom

ABSTRACT

This paper presents the study of a two-degree-of-freedom (2DoF) stacked piezoelectric energy harvester (SPEH). The high performance of the 2DoF SPEH is achieved by the frequency up-conversion mechanism, which is realized by introducing a mechanical limiter. A theoretical model of the 2DoF SPEH is developed. A piecewise linear function describes the impact interaction that incurs the frequency up-conversion phenomenon. The approximated analytical solution is derived using the averaging method. Moreover, an equivalent circuit model (ECM) is established to capture the dynamic characteristics of the SPEH. Experiments are conducted to validate the theoretical and ECM models. The effects of system parameters on the SPEH's output performance are investigated. Due to the impact-induced amplitude truncation effect, the operation bandwidth of the SPEH is substantially enlarged. For instance, the bandwidth was expanded to 6.3 Hz with a sponge gasket. The 2DoF SPEH can produce an instantaneous power with a peak amplitude of 521.6 mW under an excitation of 10.8 Hz with $k = 0.098$ N/mm. Based on the parametric study results, design guidelines to improve the system for better energy harvesting performance are discussed and summarized.

1. Introduction

Environmental contamination, the greenhouse effect, and energy deficiency continue to be major worldwide concerns. Meanwhile, traditional power sources, such as chemical batteries, cannot meet the fast development of the Internet of Things (IoTs), where billions of microelectronic devices are to be deployed ubiquitously. Enormous efforts have been devoted to harvesting energy from the ambient environment, such as solar, kinetic, and geothermal energy, and converting them into electric energy to power microelectronic devices. Kinetic energy universally exists in the ambient environment in various forms, including the flexion and extension of the fingers, the vibration of railroad tracks, and the surges brought by tides. Piezoelectric [1–5], electromagnetic [6–10], electrostatic [11–13], and triboelectric [14–16] mechanisms are the common methods to realize energy conversion; thus, they have been widely adopted in the design of different kinds of energy harvesters. Some researchers proposed combining different mechanisms to achieve hybrid systems [17–20]. Compared with other methods, the high-power density and more straightforward structural design logic of piezoelectric transduction have attracted substantial attention from researchers in this field [21–23].

Piezoelectric energy harvesters (PEHs) often operate in three modes: bending [24], torsion [25], and compression [26]. The piezoelectric materials correspondingly work in d_{31}, d_{15}, and d_{33} modes, respectively. It is well known that the piezoelectric coefficient d_{33} is almost two times greater than that of d_{31} [27]; therefore, making a PEH operate in the 33 mode should lead to a superior design. A piezoelectric stack typically comprises multiple layers working in 33-mode [28–30]. PEHs in 31 mode are widely integrated into cantilever beam types [31–34]. Given the same geometric dimensions, the power output of a stacked PEH (SPEH) is often higher than that of a cantilever-type PEH [35].

In addition to the benefit of producing a higher power output, the piezoelectric stacks are characterized by greater strengths and can, therefore, withstand higher stress than piezoelectric patches used in the 31 mode [36]. In other words, the piezoelectric stacks are more suitable for the application in the environment under heavy loads, such as harnessing mechanical energy from road surfaces [37–42]. Song et al. [43] demonstrated an integrated walkway PEH that could generate a

* Corresponding author.
E-mail address: guobiao.hu@ntu.edu.sg (G. Hu).

https://doi.org/10.1016/j.ijmecsci.2022.107299
Received 13 January 2022; Received in revised form 29 March 2022; Accepted 18 April 2022
Available online 20 April 2022

maximum power of 148.38 mW. It could collect sufficient energy to trigger a Bluetooth sensor after 22 steps of a 60 kg male. Cao et al. [44] placed a pressure fluctuation-based energy harvester in a pipeline system. It could generate an open-circuit voltage of 25.97 mV with an interface area of 50.24 mm^2. Yang et al. [45] developed a SPEH to harness energy from the pavement. The open-circuit peak voltage of the PEH reached 280 V under a 4.41 kN load. The lifespan of the stacked PEH was tested to be more than 100,000 cycles. Moure et al. [46] integrated 30,000 piezoelectric stacks into an asphalt pavement of 100 metres. When a vehicle passed through at a speed of 100 km/h, the 30,000 piezoelectric stacks could generate an average power of 0.252 W.

A reliable theoretical model can describe the dynamic behaviours of PEHs [47,48], thereby elucidating the electromechanical coupling behaviour, predicting the output performance, and guiding the system optimization [49–53]. Qian et al. [31] built an electromechanical coupling model in ANSYS and validated it experimentally. They also presented a distributed-parameter model of a multilayer-stacked PEH for predicting output performance under random excitations [54]. Chen et al. [55] developed a finite element (FE) model for a portable PEH and presented the experimental validation. Zhao and Erturk [56] established an electromechanical model of a piezoelectric stack to predict its dynamic behaviour under uniaxial pressure loads within the off-resonant bandwidth. Shevtsov and Flek [57] developed a lumped parameter model based on a 3D FE model of a stack-based PEH. The simplified lumped parameter model has a much higher computational efficiency, thus easing iterative calculations towards system optimization.

However, due to the high strength, the resonant frequencies of piezoelectric stacks are often much higher than environmental vibration frequencies. According to the fundamentals of vibration energy harvesting, once the excitation frequency deviates from the resonant frequency of a PEH, the output power will drastically decrease. In recent years, many efforts have been devoted to broadening the working bandwidth of SPEHs. The proposed multi-stable [58,59] and multi-degree-of-freedom [60–62] structures operate in still relatively high resonant frequencies. The frequency up-conversion mechanism can convert low-frequency excitations into high-frequency responses. The frequency up-conversion technique can be adopted to adapt piezoelectric stacks for low-frequency energy conversion by enhancing the power output and enlarging the bandwidth [63–67]. Most existing research focuses on exploring the application of the frequency up-conversion technique in the design of cantilever-type PEHs working in the 31 mode. Zhang and Qin [68] changed the working frequency of a harvester from 74.75 Hz to 106 Hz by just adjusting the rope margin. Panthongsya et al. [69] developed a frequency up-conversion PEH that consisted of 24 cantilever beams. The effect of the frequency up-conversion mechanism on SPEHs has rarely been studied.

This paper demonstrates the structural design, theoretical analysis, and experimental study of a two-degree-of-freedom (2DoF) SPEH that employs the frequency up-conversion technique. The key novelties and contributions are: First, an electromechanical model is established, and the theoretical solution is derived. Moreover, an equivalent circuit model (ECM) of the 2DoF SPEH by considering the frequency up-conversion mechanism is established. Experiments are conducted to validate the theoretical and ECM simulation results. In addition, the effects of the system parameters on the energy harvesting performance of the 2DoF SPEH are thoroughly investigated.

2. Theoretical model and approximated analytical solution

Piezoelectric stacks can withstand greater loads than piezoelectric patches used in the 31mode. The force on the piezo-stack can reach hundreds of newtons [70–72] as the combination of a power amplifier and the impact mode under a large excitation. A structural configuration of an SPEH, as shown in Fig. 1, is proposed in this paper. The SPEH is comprised of a spring, a mechanical limiter, a force amplifier, a proof mass, an axle, and piezoelectric stacks. The force amplification mechanism generates a micro elastic-deformation induced by the impact of the proof mass. This section presents the theoretical modelling of the proposed SPEH and the derivation of its approximated analytical solution.

The system presented in Fig. 1 can be simplified and represented as the model illustrated in Fig. 2(a). Fig. 2(b) shows the corresponding equivalent lumped parameter model. m_1 denotes the proof mass. m_2

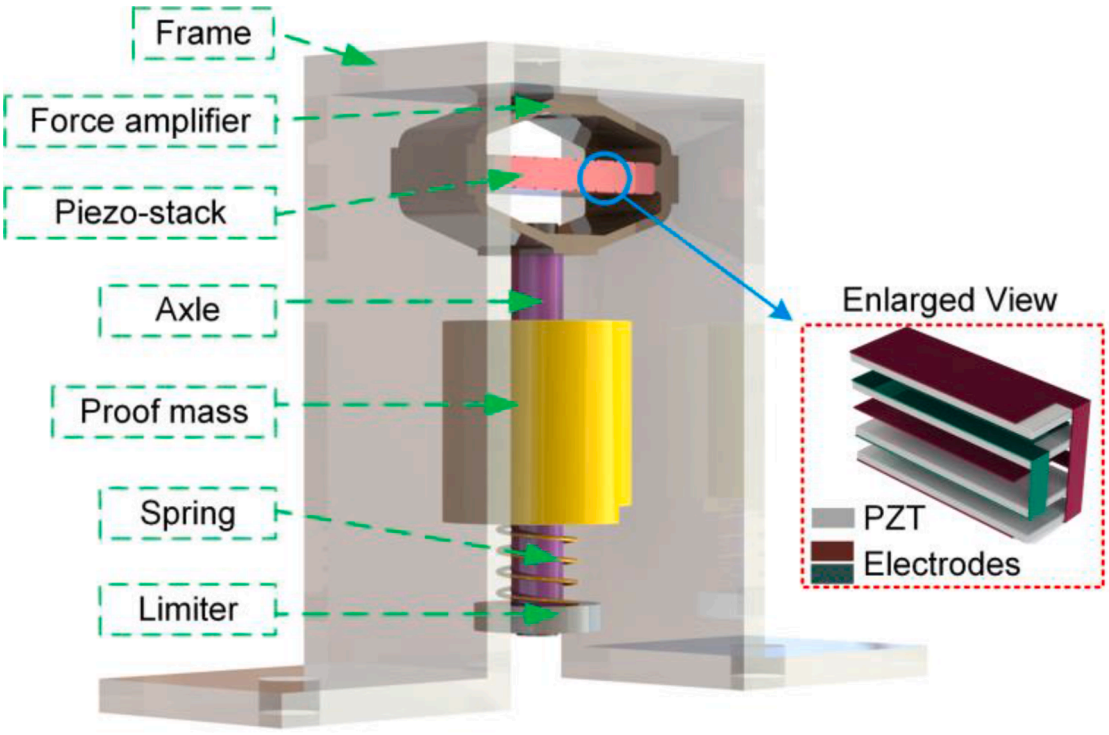

Fig. 1. The structural configuration of the proposed SPEH.

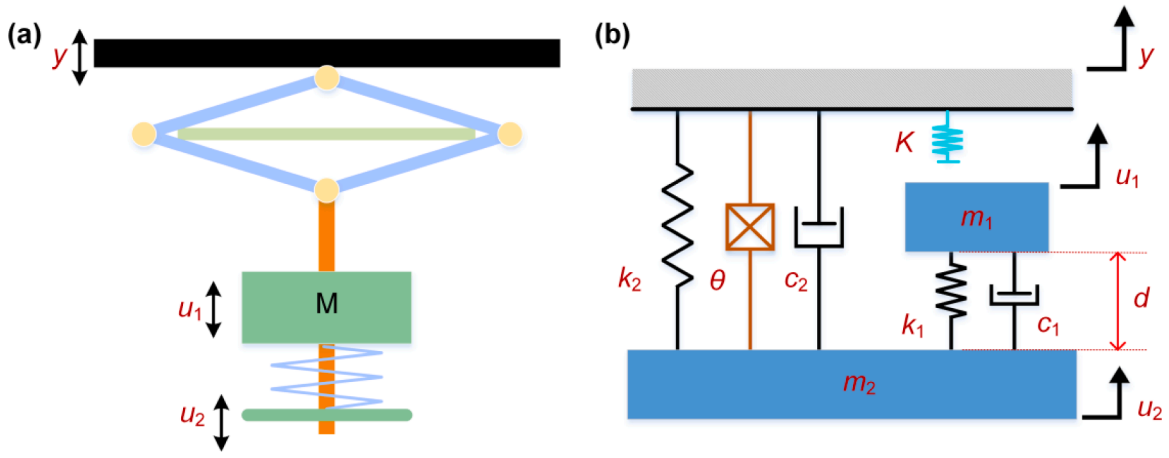

Fig. 2. Schematic of (a) the physical prototype; (b) the equivalent lumped 2DoF model.

represents the equivalent mass of the axle, spring limiter, force amplifier, and piezo-stack. k_i and c_i ($i = 1, 2$) denote the equivalent stiffness and damping coefficient, respectively. The subscripts 1 and 2 denote the degrees of freedom related to m_1 and m_2, respectively. The governing equations of the 2DoF SPEH can be written as:

$$m_1\ddot{u}_1(t) + c_1(\dot{u}_1(t) - \dot{u}_2(t)) + k_1(u_1(t) - u_2(t)) + H(u_1(t), u_2(t)) = -m_1\ddot{y}(t) \tag{1}$$

$$\begin{aligned} &m_2\ddot{u}_2(t) + c_2\dot{u}_2(t) + k_2u_2(t) + c_1(\dot{u}_2(t) - \dot{u}_1(t)) \\ &+k_1(u_2(t) - u_1(t)) - H(u_1(t), u_2(t)) + \theta v(t) = -m_2\ddot{y}(t) \end{aligned} \tag{2}$$

$$\frac{v(t)}{R} + C_p\dot{v}(t) = \theta\dot{u}_2(t) \tag{3}$$

in which u_i ($i = 1, 2$), y, v, R, C_p, and θ denote the displacements of the equivalent masses m_1 and m_2 relative to the base, the base excitation displacement, the output voltage, the external load resistance, the capacitance of the piezo-stack, and the electromechanical coupling coefficient, respectively. The impact-induced nonlinear force is described by a piecewise linear function as:

$$H(u_1(t), u_2(t)) = \begin{cases} K(u_1(t) - u_2(t) + d) & u_1(t) - u_2(t) < -d \\ 0 & u_1(t) - u_2(t) \geq -d \end{cases} \tag{4}$$

where K denotes the collision stiffness during the impact.

Before solving the equations, it is noted that Eq. (3) does not involve the nonlinear term and contains only two unknown variables, i.e., $v(t)$ and $u_2(t)$. Through Eq. (3), $v(t)$ can be represented by $u_2(t)$.

$$v(t) = \frac{R\theta}{1 + \omega^2R^2C_p^2}\dot{u}_2(t) + \frac{\omega^2R^2C_p^2\theta}{1 + \omega^2R^2C_p^2}u_2(t) \tag{5}$$

By defining $c_2' = c_2 + \frac{R\theta^2}{1+\omega^2R^2C_p^2}$, $k_2' = k_2 + \frac{\omega^2R^2C_p^2\theta}{1+\omega^2R^2C_p^2}$, Eq. (2) becomes:

$$\begin{aligned} &m_2\ddot{u}_2(t) + c'_2\dot{u}_2(t) + k'_2u_2(t) + c_1(\dot{u}_2(t) - \dot{u}_1(t)) \\ &+k_1(u_2(t) - u_1(t)) - p(u_1(t), u_2(t)) = -m_2\ddot{y}(t) \end{aligned} \tag{6}$$

In this way, the unknown variable $v(t)$ can be eliminated from the governing equations, the number of the governing equations can be reduced, and the problem can be greatly simplified. Let $x_1(t) = u_1(t)$ and $x_2(t) = u_1(t) - u_2(t)$, the governing equations, i.e., Eqs. (1), (6), become:

$$m_1\ddot{x}_1(t) + c_1\dot{x}_2(t) + k_1x_2(t) + H(u_1(t), u_2(t)) = -m_1\ddot{y}(t) \tag{7}$$

$$\begin{aligned} &m_2\left(\ddot{x}_1(t) - \ddot{x}_2(t)\right) + c'_2(\dot{x}_1(t) - \dot{x}_2(t)) + k'_2(x_1(t) - x_2(t)) \\ &-c_1\dot{x}_2(t) - k_1x_2(t) - H(x_1(t), x_2(t)) = -m_2\ddot{y}(t) \end{aligned} \tag{8}$$

Manipulating Eqs. (7) & (8) to eliminate $\ddot{x}_1(t)$ from Eq. (8) gives:

$$\begin{aligned} &m_2\ddot{x}_2(t) + c'_2(\dot{x}_2(t) - \dot{x}_1(t)) + k'_2(x_2(t) - x_1(t)) \\ &+\left(1 + \frac{m_2}{m_1}\right)c_1\dot{x}_2(t) + \left(1 + \frac{m_2}{m_1}\right)k_1x_2(t) + \left(1 + \frac{m_2}{m_1}\right)H(x_1(t), x_2(t)) = 0 \end{aligned} \tag{9}$$

The piecewise linear impact stiffness, i.e., (4), becomes

$$H(x_1(t), x_2(t)) = \begin{cases} K(x_2(t) + d) & x_2(t) \leq -d \\ 0 & x_2(t) > -d \end{cases} \tag{10}$$

The averaging method is employed to derive the analytical solution to Eqs. (8), (9). Without loss of generality, the base excitation is assumed to be in the form as [71,73]:

$$y(t) = Y\cos(\omega t) \tag{11}$$

The displacements are assumed in similar forms as:

$$\begin{cases} x_1(t) = a_1(t)\cos(\omega t - \theta_1(t)) \\ x_2(t) = a_2(t)\cos(\omega t - \theta_2(t)) \end{cases} \tag{12}$$

where $a_1(t)$,$a_2(t)$,$\theta_1(t)$,*and*$\theta_2(t)$ are slowly time-varying parameters. Hence, we can further propose the assumption that the velocities are in the concise forms as:

$$\begin{cases} \dot{x}_1(t) = -a_1(t)\omega\sin(\omega t - \theta_1(t)) \\ \dot{x}_2(t) = -a_2(t)\omega\sin(\omega t - \theta_2(t)) \end{cases} \tag{13}$$

Differentiating Eq. (12), then equalling to Eq. (13) yields:

$$\begin{cases} \dot{a}_1(t)\cos(\omega t - \theta_1(t)) + a_1(t)\dot{\theta}_1(t)\sin(\omega t - \theta_1(t)) = 0 \\ a_2(t)\cos(\omega t - \theta_2(t)) + a_2(t)\dot{\theta}_2(t)\sin(\omega t - \theta_2(t)) = 0 \end{cases} \tag{14}$$

On the other hand, substituting Eqs. (11)–(13) into Eqs. (7), (9) gives:

$$\begin{aligned} &\dot{a}_1(t)\sin(\omega t - \theta_1(t)) - a_1(t)\dot{\theta}_1(t)\cos(\omega t - \theta_1(t)) \\ &= \frac{1}{\omega}\begin{bmatrix} -Y\cos(\omega t)\omega^2 - a_1(t)\cos(\omega t - \theta_1(t))\omega^2 \\ -\frac{c_1}{m_1}a_2(t)\omega\sin(\omega t - \theta_2(t)) \\ +\frac{k_1}{m_1}a_2(t)\cos(\omega t - \theta_2(t)) + \frac{H(a_2(t), \theta_2(t))}{m_1} \end{bmatrix} = f_1 \end{aligned} \tag{15}$$

$$\dot{a}_2(t)\sin(\omega t-\theta_2(t))-a_2(t)\dot{\theta}_2(t)\cos(\omega t-\theta_2(t))=$$

$$\frac{1}{\omega}\begin{bmatrix}-a_2(t)\cos(\omega t-\theta_2(t))\omega^2+\frac{c'_2}{m_2}a_1(t)\omega\sin(\omega t-\theta_1(t))\\ -\frac{c_1}{m_2}a_2(t)\omega\sin(\omega t-\theta_2(t))-\frac{c_1}{m_1}a_2(t)\omega\sin(\omega t-\theta_2(t))\\ -\frac{c'_2}{m_2}a_2(t)\omega\sin(\omega t-\theta_2(t))-\frac{k'_2}{m_2}a_1(t)\cos(\omega t-\theta_1(t))\\ +\frac{k_1}{m_2}a_2(t)\cos(\omega t-\theta_2(t))+\frac{k_1}{m_1}a_2(t)\cos(\omega t-\theta_2(t))\\ +\frac{k'_2}{m_2}a_2(t)\cos(\omega t-\theta_2(t))+\left(\frac{1}{m_1}+\frac{1}{m_2}\right)H(a_2(t),\theta_2(t))\end{bmatrix}=f_2 \tag{16}$$

By defining $\phi_1=\omega t-\theta_1(t)$ and substituting it into Eq. (15), one obtains

$$f_1=\frac{1}{\omega}\begin{bmatrix}-Y\cos(\phi_1+\theta_1)\omega^2-a_1\cos(\phi_1)\omega^2-\frac{c_1}{m_1}a_2\omega\sin(\phi_1-\theta_{21})\\ +\frac{k_1}{m_1}a_2\cos(\phi_1-\theta_{21})+H_1\end{bmatrix} \tag{17}$$

where $\theta_{21}=\theta_2(t)-\theta_1(t)$, and

$$H_1=\begin{cases}K[a_2\cos(\phi_1-\theta_{21})+a_2\cos\phi_0] & \pi+\theta_{21}-\phi_0\le\phi_1\le\pi+\theta_{21}+\phi_0\\ 0 & \theta_{21}\le\phi_1<\pi+\theta_{21}-\phi_0\\ & and\ \pi+\theta_{21}+\phi_0<\phi_1\le 2\pi+\theta_{21}\end{cases} \tag{18}$$

By defining $\phi_2=\omega t-\theta_2(t)$ and substituting it into Eq. (16), one obtains

$$f_2=\frac{1}{\omega}\begin{bmatrix}-a_2\cos(\phi_2)\omega^2+\frac{c'_2}{m_2}a_1\omega\sin(\phi_2+\theta_2-\theta_1)-\frac{c_1}{m_2}a_2\omega\sin(\phi_2)\\ -\frac{c_1}{m_1}a_2\omega\sin(\phi_2)-\frac{c'_2}{m_2}a_2\omega\sin(\phi_2)-\frac{k'_2}{m_2}a_1\cos(\phi_2+\theta_2-\theta_1)\\ +\frac{k_1}{m_2}a_2\cos(\phi_2)+\frac{k_1}{m_1}a_2\cos(\phi_2)+\frac{k'_2}{m_2}a_2\cos(\phi_2)+\left(\frac{1}{m_1}+\frac{1}{m_2}\right)H_2\end{bmatrix} \tag{19}$$

in which

$$H_2=\begin{cases}K[a_2\cos(\phi_2)+a_2\cos\phi_0] & \pi-\phi_0\le\phi_2\le\pi+\phi_0\\ 0 & 0\le\phi_2<\pi-\phi_0\ and\ \pi+\phi_0<\phi_2\le 2\pi\end{cases} \tag{20}$$

Solving Eqs. (14) & (15), one obtains:

$$\begin{cases}\dot{a}_1=f_1\sin\phi_1\\ \dot{\theta}_1=-\frac{1}{a_1}f_1\cos\phi_1\\ \dot{a}_2=f_2\sin\phi_2\\ \dot{\theta}_2=-\frac{1}{a_2}f_2\cos\phi_2\end{cases} \tag{21}$$

As a_1, a_2, θ_1, and θ_2 are slowly time-varying parameters, $\dot{a}_1$, $\dot{a}_2$, $\dot{\theta}_1$, and $\dot{\theta}_2$ can be considered to be zero.

$$\begin{cases}-\frac{c_1a_2\pi}{m_1}\cos(\theta_{21})+\omega Y\pi\sin(\theta_1)+\frac{1}{\omega}\left[\frac{Ka_2\phi_0}{m_1}+\frac{k_1a_2\pi}{m_1}-\frac{Ka_2\sin(\phi_0)\cos(\phi_0)}{m_1}\right]\sin(\theta_{21})=0\\ -\omega Y\pi\cos(\theta_1)+\frac{1}{\omega}\left[\frac{Ka_2\phi_0}{m_1}+\frac{k_1a_2\pi}{m_1}-\frac{Ka_2\sin(\phi_0)\cos(\phi_0)}{m_1}\right]\cos(\theta_{21})+\frac{a_2c_1\pi}{m_1}\sin(\theta_{21})-\omega a_1\pi=0\\ \frac{c'_2a_1\pi}{m_2}\cos(\theta_{21})+\frac{k'_2a_1\pi}{m_2\omega}\sin(\theta_{21})-\left(\frac{c_1a_2\pi}{m_1}+\frac{c_1a_2\pi}{m_2}+\frac{c'_2a_2\pi}{m_2}\right)=0\\ \frac{c'_2a_1\pi}{m_2}\sin(\theta_{21})-\frac{k'_2a_1\pi}{m_2\omega}\cos(\theta_{21})+\frac{1}{\omega}\begin{bmatrix}\frac{k_1a_2\pi}{m_1}+\frac{Ka_2\phi_0}{m_1}+\frac{k_1a_2\pi}{m_2}+\frac{k'_2a_2\pi}{m_2}+\frac{Ka_2\phi_0}{m_2}\\ -\omega^2a_2\pi-\frac{Ka_2\sin(\phi_0)\cos(\phi_0)}{m_2}-\frac{Ka_2\sin(\phi_0)\cos(\phi_0)}{m_1}\end{bmatrix}=0\end{cases} \tag{22}$$

Eliminating θ_1 and θ_2 from Eq. (22) yields:

$$\begin{cases}\frac{(r_{10}r_{11}-r_{13}r_8)^2}{(r_{11}r_9-r_{12}r_8)^2}+\frac{(r_{10}r_{12}-r_{13}r_9)^2}{(r_{11}r_9-r_{12}r_8)^2}=1\\ \frac{\left(\begin{matrix}r_{10}r_{11}r_6-r_{10}r_{12}r_5-r_{11}r_7r_9\\ +r_{12}r_7r_8+r_{13}r_5r_9-r_{13}r_6r_8\end{matrix}\right)^2}{r_4{}^2(r_{11}r_9-r_{12}r_8)^2}+\frac{(r_{10}r_{11}r_3-r_{10}r_{12}r_2+r_{13}r_2r_9-r_{13}r_3r_8)^2}{r_1{}^2(r_{11}r_9-r_{12}r_8)^2}=1\end{cases} \tag{23}$$

where $r_1=\omega Y\pi$, $r_2=\frac{Ka_2\phi_0}{\omega m_1}+\frac{k_1a_2\pi}{\omega m_1}-\frac{Ka_2\sin(\phi_0)\cos(\phi_0)}{\omega m_1}$, $r_3=-\frac{c_1a_2\pi}{m_1}$, $r_4=-r_1$, $r_5=-r_3$, $r_6=r_2$, $r_7=-\omega a_1\pi$, $r_8=\frac{k'_2a_1\pi}{m_2\omega}$, $r_9=\frac{c'_2a_1\pi}{m_2}$, $r_{10}=-\left(\frac{c_1}{m_1}+\frac{c_1+c'_2}{m_2}\right)a_2\pi$, $r_11=r_9$, $r_12=r_8$, and $r_{13}=$

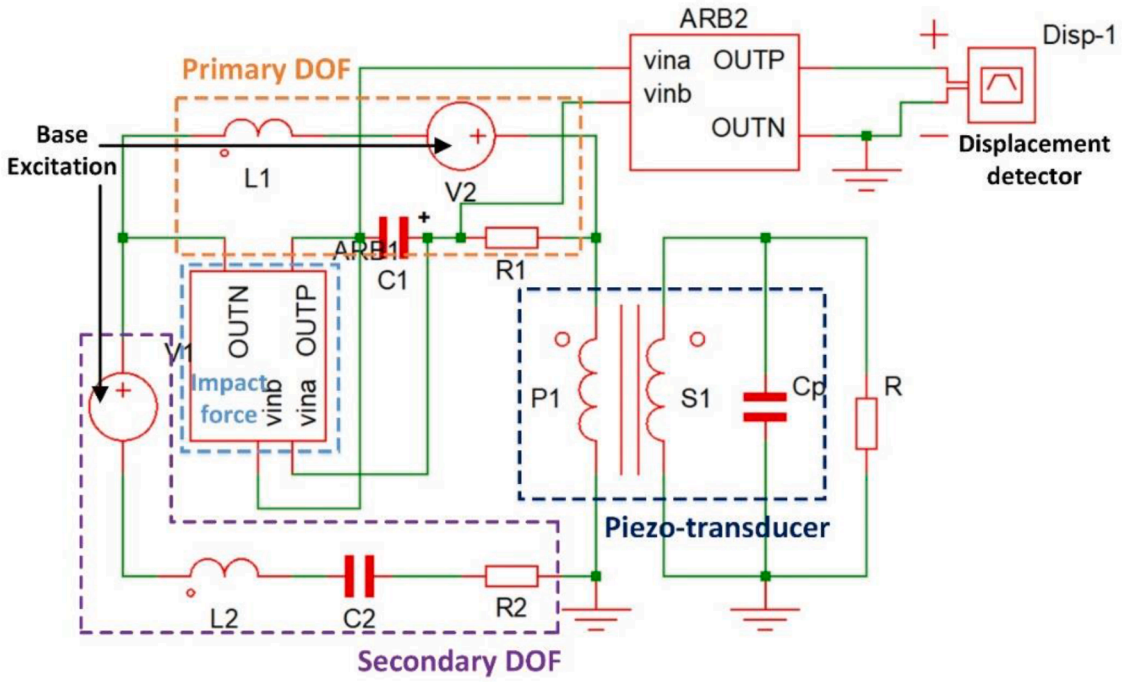

Fig. 3. Equivalent circuit model of the 2DoF SPEH.

$$\frac{1}{\omega}\begin{bmatrix} \frac{k_1 a_2 \pi}{m_1} + \frac{K a_2 \phi_0}{m_1} + \frac{k_1 a_2 \pi}{m_2} + \frac{k'_2 a_2 \pi}{m_2} + \frac{K a_2 \phi_0}{m_2} - \omega^2 a_2 \pi \\ -\frac{K a_2 \sin(\phi_0)\cos(\phi_0)}{m_2} - \frac{K a_2 \sin(\phi_0)\cos(\phi_0)}{m_1} \end{bmatrix}.$$

By solving Eq. (23), one obtains the solution to a_1 and a_2. Note that a_2 is the amplitude of $x_2(t)$. However, Eq. (5) indicates that the output voltage is proportional to the $u_2(t)$. According to the definition, it is known that:

$$u_2(t) = x_1(t) - x_2(t) = a_1\cos(\omega t - \theta_1) - a_2\cos(\omega t - \theta_2) \tag{24}$$

Therefore, the amplitude of $u_2(t)$ can be derived:

$$U_2 = \sqrt{(a_1\cos(\theta_1) - a_2\cos(\theta_2))^2 + (a_1\sin(\theta_1) - a_2\sin(\theta_2))^2} \tag{25}$$

where

$$\begin{cases} \sin(\theta_1) = \dfrac{r_{10}r_{11}r_3 - r_{10}r_{12}r_2 + r_{13}r_2r_9 - r_{13}r_3r_8}{r_1(r_{11}r_9 - r_{12}r_8)} \\ \cos(\theta_1) = \dfrac{r_{10}r_{11}r_6 - r_{10}r_{12}r_5 - r_{11}r_7r_9 + r_{12}r_7r_8 + r_{13}r_5r_9 - r_{13}r_6r_8}{r_4(r_{11}r_9 - r_{12}r_8)} \\ \sin(\theta_2) = \dfrac{r_{10}r_{12} - r_{13}r_9}{r_{11}r_9 - r_{12}r_8} \\ \cos(\theta_2) = -\dfrac{r_{10}r_{11} - r_{13}r_8}{r_{11}r_9 - r_{12}r_8} \end{cases}$$

Table 1
System parameters of the 2DoF SPEH.

Mechanical parameters	Values	Mechanical parameters	Values
Effective mass m_1 (g)	29	Electromechanical coupling θ (N/V)	0.054
Effective mass m_2 (g)	23.3	Capacitance C_p (μF)	1.732
Effective stiffness k_1 (N/m)	490	Base excitation (m/s^2)	7.35
Effective stiffness k_2 (N/m)	1.449×10^6	Impact stiffness (N/m)	500,000
Damping ratio ζ_1	0.008	Initial gap (mm)	14.4
Damping ratio ζ_2	0.006	Load resistance (Ω)	10^{12}

Finally, the voltage amplitude can be obtained:

$$V = \left|\frac{i\omega R\theta}{1 + i\omega RC_p}\right| U_2 \tag{26}$$

3. Equivalent circuit model

In this section, an equivalent circuit model of the 2DoF SPEH, as shown in Fig. 3, is developed using the commercial circuit simulation software SIMetrix to verify the analytical solution derived in the previous section. According to electromechanical analogies, mechanical quantities, such as force, velocity, and displacement, are equivalent to the electrical quantities of voltage, current, and charge, respectively. The resistor, inductor, and capacitor in the electrical domain can represent the damper, mass, and spring in the mechanical domain. The piezoelectric harvester can be represented as integrating a capacitor and an ideal transformer connected in parallel. The base excitation is simulated by a voltage source. A nonlinear transfer function generates the impact force. The part on the left-hand side of the transformer in Fig. 3 represents the mechanical domain, and the right-hand side represents the circuit domain. The left-hand side circuit is composed of two branches/loops since the mechanical domain of the energy harvester is a two-degree-of-freedom structure. A transient simulation should be carried out until the result reaches a steady state. A voltage probe can be placed to measure the terminal voltage of the resistance directly. Moreover, one can measure the voltages across the capacitors and calculate the accumulated charges to know the displacement information. More detailed procedures for establishing the equivalent circuit model of a piezoelectric energy harvester can refer to [74,75].

For the given system parameters listed in Table 1, the equivalent circuit simulation results are presented in Fig. 4. The approximated analytical results are also plotted out for comparison. It can be seen that the voltage output profile obtained by the ECM simulation is asymmetric since the impact occurs at only one side of the 2DoF SPEH. Therefore, the ECM model well captures the dynamic characteristics of the 2DoF SPEH based on the frequency-up conversion mechanism. Unfortunately, the averaging method employed is limited to the first-order approximation. The response solutions assumed at the beginning are symmetric.

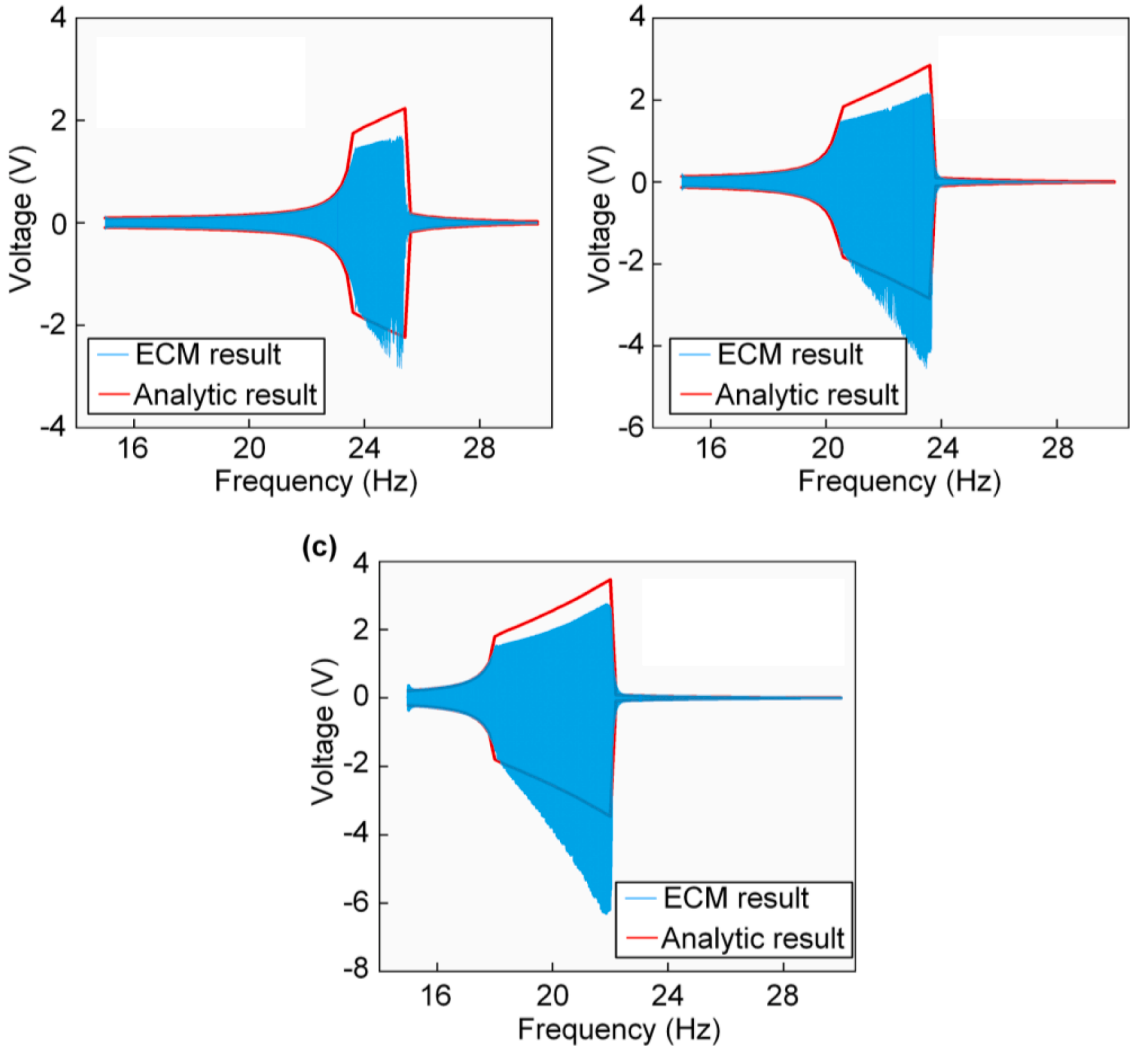

Fig. 4. Comparison of the theoretical and equivalent circuit simulation results. (a) the comparison of $m = 21.6$ g case; (b) the comparison of $m = 29$ g case; (c) the comparison of $m = 37.2$ g case.

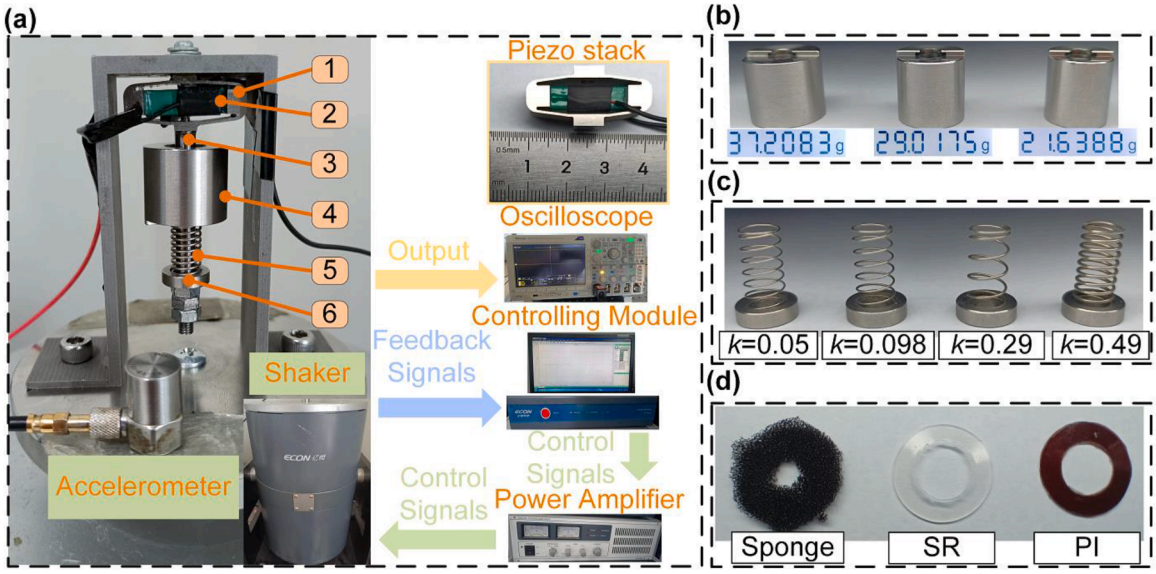

Fig. 5. Experiment setup: (a) Experiment setup with a fabrication prototype. The labels of the key elements are 1. Force amplifier, 2. Piezo stack, 3. Axle, 4. Proof mass, 5. Spring, 6. Limiter; (b) The proof masses of 37.2, 29, and 21.6 g; (c) The springs of $k = 0.05$, $k = 0.098$, $k = 0.29$, and $k = 0.49$ N/mm; (d) The gaskets made of sponge, silicone rubber (SR), and polyimide (PI) materials.

Table 2
Geometric and material parameters of the fabricated physical prototype.

	Description	Value
SPEH	Dimension (mm×mm×mm)	20 × 26.9 × 64
Piezoelectric stack	Material	PZT-5H
	Number of layers	180
	Young's modulus (GPa)	62
	Piezoelectric constant g_{33} (10^{-3} V m/N)	12.5
	Capacitance (μF)	1.732
	Density (kg/m^3)	8000
	Dimension (mm×mm×mm)	5 × 5 × 18
Proof mass	Diameter (mm)	20, 18, 16
	Mass (g)	37.2, 29, 21.6
Spring	Stiffness (N/mm)	0.05, 0.098, 0.29, 0.49, 0.98
	External diameter (mm)	8
	Free length (mm)	15
GASKET	Stiffness (N/mm)	2.15, 209.1, 364

Thus, the analytical result exhibits a symmetric profile. Though the analytical amplitudes cannot precisely match the simulation results, the overall profile, i.e., the enlarged bandwidth region, qualitatively agrees with the simulation results. Therefore, the approximated analytical method is verified. Both the ECM simulation and approximated analytical results indicate that with the increase of the proof mass, the resonant frequency of the 2DoF SPEH moves toward a low-frequency direction. Moreover, with the increase of the proof mass, the resonant region becomes wider, i.e., the effective bandwidth is enlarged, and the voltage amplitudes over the bandwidth are increased.

4. Experimental test and result discussion

This section presents the experimental study to validate the results obtained from the equivalent circuit simulation. Fig. 5 shows the experiment setup and the fabricated prototype. As demonstrated in Fig. 5(a), the fabricated prototype consists of 6 components: a force amplifier, a piezo-stack, an axle, a proof mass, a spring, and a limiter. The proof mass, force amplifier, and limiter were all made of stainless steel (SS-304). The material used for the axle is 45# steel. Gaskets made of different materials (sponge, silicone rubber (SR), and polyimide (PI)) are used as impact buffers. Note that the stiffness of the sponge significantly increases when it is under compression. Table 2 lists the geometric and material parameters of the fabricated physical prototype. Different proof masses, springs, and gaskets were tested to investigate their effects on the output performance of the fabricated prototype. The fabricated prototype was fixed on a frame attached to the shaker (Econ. E-JZK-50). A controller (Econ. VT-9002) wasused to produce a customized excitation signal. An amplifier (Econ. E5874A) amplifies the excitation signal and drives the shaker to generate the desired excitation. An accelerometer (Econ. EAYD-181) was attached to the shaker to monitor the excitation, forming a closed-loop control of the shaker. The voltage output from the prototype energy harvester was measured and recorded by an oscilloscope (Tektronix MDO3024)

4.1. ECM model validation

In this section, a comparative analysis is performed between the ECM simulation and experimental results of the 2DoF SPEH to validate the ECM model established in Section 3. Given the spring stiffness of 0.49 N/mm, Fig. 6 compares the ECM simulation and experimental results of the voltage output in the frequency domain from the prototype energy harvester. Over the frequency range under investigation, the excitation acceleration is controlled constantly at 0.75 G (G is the gravitational constant). The piezo stack is under open-circuit condition. Note that the voltage profile is asymmetric since the impact-induced amplitude truncation effect only occurs at one side of the 2DoF SPEH. Due to the presence of the limiter, the frequency response of the 2DoF SPEH exhibits a hardening phenomenon. As a consequence, the bandwidth of the 2DoF SPEH is significantly enlarged to 18.3~24.3 Hz (Fig. 6(a)) when the proof mass equals 37.2 g. When the proof mass decreases to 29 g, the bandwidth becomes 20.4~26.1 Hz (Fig. 6(b)). Similarly, the simulation result profile is also asymmetric, and the effective bandwidth is widened. When the proof mass is 37.2 g, the bandwidth predicted by the simulation result is approximately 18.1~24.4 Hz (Fig. 6(a)). When the proof mass is 29 g, the bandwidth increases to 20.3~26.3 Hz (Fig. 6(b)). Hence, the ECM result agrees with the experimental result well.

Subsequently, the time-history voltage outputs of the prototype energy harvester predicted by ECM simulation and measured in the experiment are presented in Fig. 7 for further comparison. The excitation acceleration is controlled at 0.75 G, and the external excitation frequency is fixed at 22.3 Hz. The peak-peak voltage and the high-frequency component of the experimental result are about 4.9 V and 1269 Hz, respectively. The analytical results of the peak-to-peak voltage and the high-frequency components are 4.8 V and 1280 Hz, respectively. Considering the complexity of the physical model and many uncertain factors in the experiment, the ECM simulation result can be regarded as validated.

4.2. Parametric study

This section discusses the effects of the system parameters (i.e., proof mass, spring stiffness, and impact stiffness) on the energy harvesting performance. A series of parametric experiments are carried out to investigate the effects of system parameters on the frequency and time-domain voltage responses of the energy harvester. Working bandwidth is a crucial figure of merit to evaluate the performance of an energy harvester. A larger bandwidth indicates that the energy harvester can harness vibration energy from the ambient environment over a broader

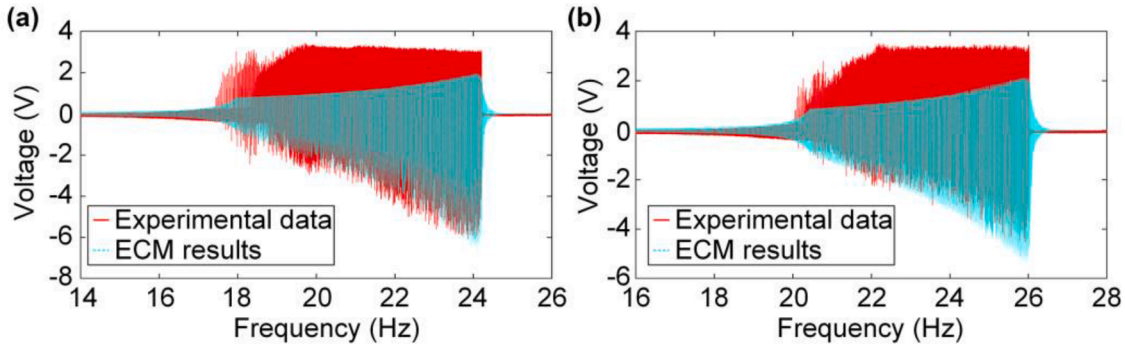

Fig. 6. Comparison of the frequency-domain voltage output results from the experiment and the analytical prediction. The excitation acceleration is controlled at 0.75 G, and the spring stiffness is 0.49 N/mm. (a) the comparison of $m = 37.2$ g case; (b) the comparison of $m = 29$ g case.

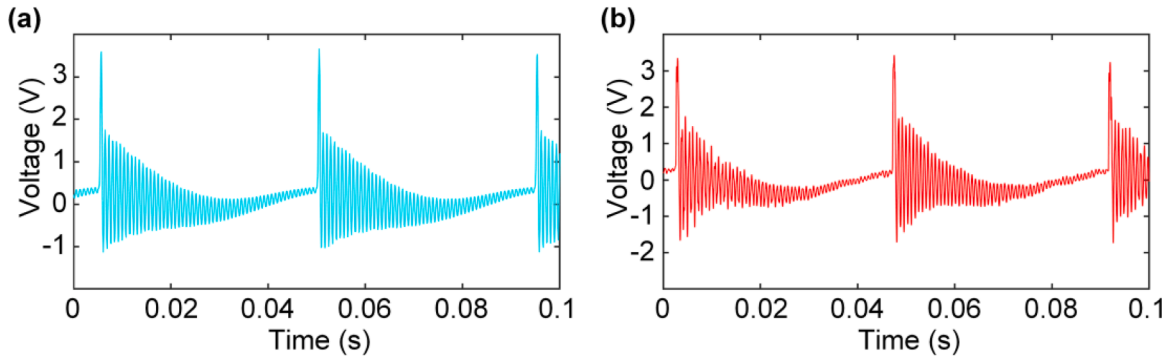

Fig. 7. Comparison of the time-domain voltage output results from the experiment and the ECM simulation. The excitation acceleration is controlled at 0.75 G, and the spring stiffness is 0.49 N/mm. (a) the time-domain voltage responses of the ECM simulation; (b) the time-domain voltage responses of the experiment.

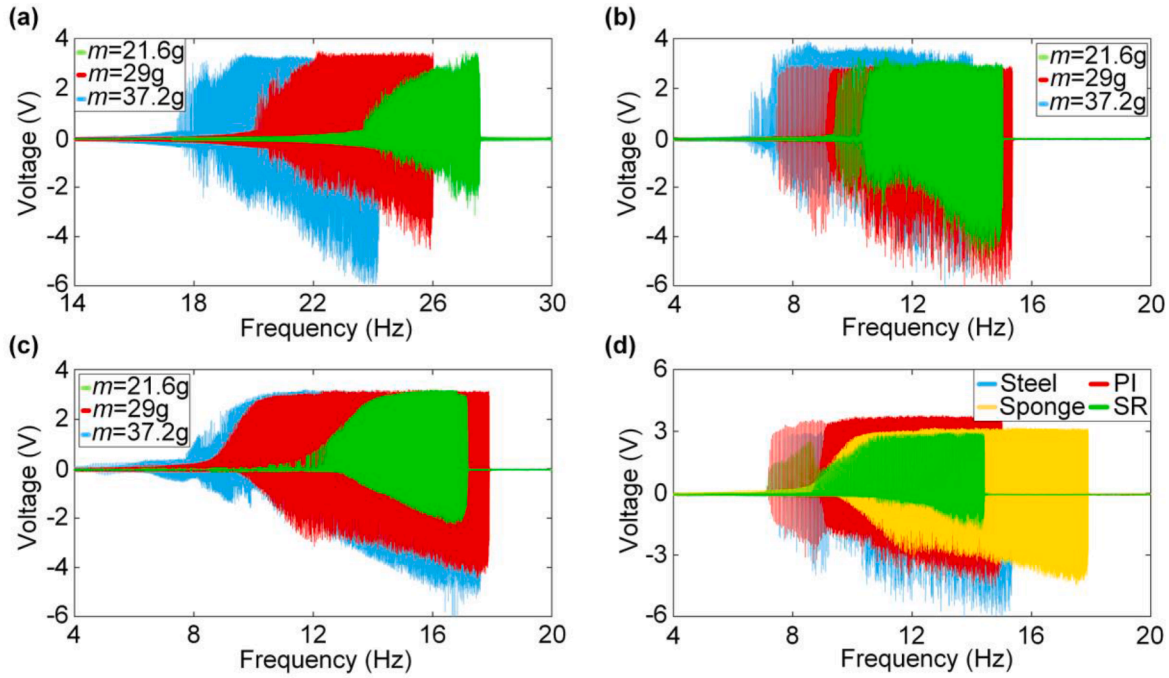

Fig. 8. Voltage responses in the frequency domain from different experiment conditions under excitation acceleration of 0.75 G. (a) The frequency-domain voltage responses of different proof masses (21.6, 29, and 37.2 g) with $k = 0.49$ N/mm without gaskets; (b) The frequency-domain voltage responses of different proof masses (21.6, 29, and 37.2 g) with $k = 0.098$ N/mm without gaskets; (c) The frequency-domain voltage responses of different proof masses (21.6, 29, and 37.2 g) with $k = 0.098$ N/mm and the sponge gasket; (d) The frequency-domain voltage responses of gaskets made of different materials (sponge, PI, and SR) with $m = 29$ g and $k = 0.098$ N/mm.

frequency spectrum. Fig. 8 presents the experimental results. With increased excitation frequency, the voltage amplitude first increases and then decreases. The voltage profiles are all asymmetric because the impact occurs only at one side of the 2DoF PEH. The voltage in the positive zone of the *y*-axis first increases when the displacement of the proof mass is small, and no impact takes place. It then remains almost constant due to the impact-induced amplitude truncation effect. The voltage in the negative zone of the *y*-axis keeps increasing until the end of the bandwidth. Due to the impact-induced amplitude truncation effect, the resonant peak is similar to being flattened; the bandwidth is thus stretched.

Fig. 8(a) shows that the resonant peak shifts toward a high-frequency direction by decreasing the proof mass. The resonant amplitude at high frequencies is smaller; therefore, the impact occurs within a narrower frequency range. When the proof mass is 21.6 g, the amplitude truncation effect is negligible, implying that impact barely occurs in the 2DoF PEH. From the broadband low-frequency energy harvester perspective, a heavier proof mass is more favourable. The results presented in Fig. 8 (a) agree with the predictions of the theory (Fig. 4). The results in Fig. 8 (b) correspond to the cases with a reduced spring stiffness of $k = 0.098$ N/mm. As the spring stiffness decreases, the resonances shift to lower-frequency ranges. Similarly, the resonant amplitudes at low frequencies are relatively large, indicating that impact can occur more easily. Therefore, the impact-induced amplitude truncation effect becomes more evident compared to the results presented in Fig. 8(a), and the bandwidth is enlarged.

Subsequently, different gaskets are installed in the 2DoF PEH as impact buffers to modify the impact behaviour effectively. Qualitatively speaking, a softer gasket should lead to a minor impact stiffness. For the same system parameters as those in Fig. 8(b), (c) illustrates the corresponding results after introducing a sponge gasket. It can be observed that the voltage response curve becomes smoother due to the sponge gasket. However, the voltage amplitudes are decreased compared to the cases without using the sponge gasket (Fig. 8(b)). By fixing the proof mass (29 g) and the spring stiffness ($k = 0.098$ N/mm), Fig. 8(d) presents the results of several cases using gaskets made of different materials.

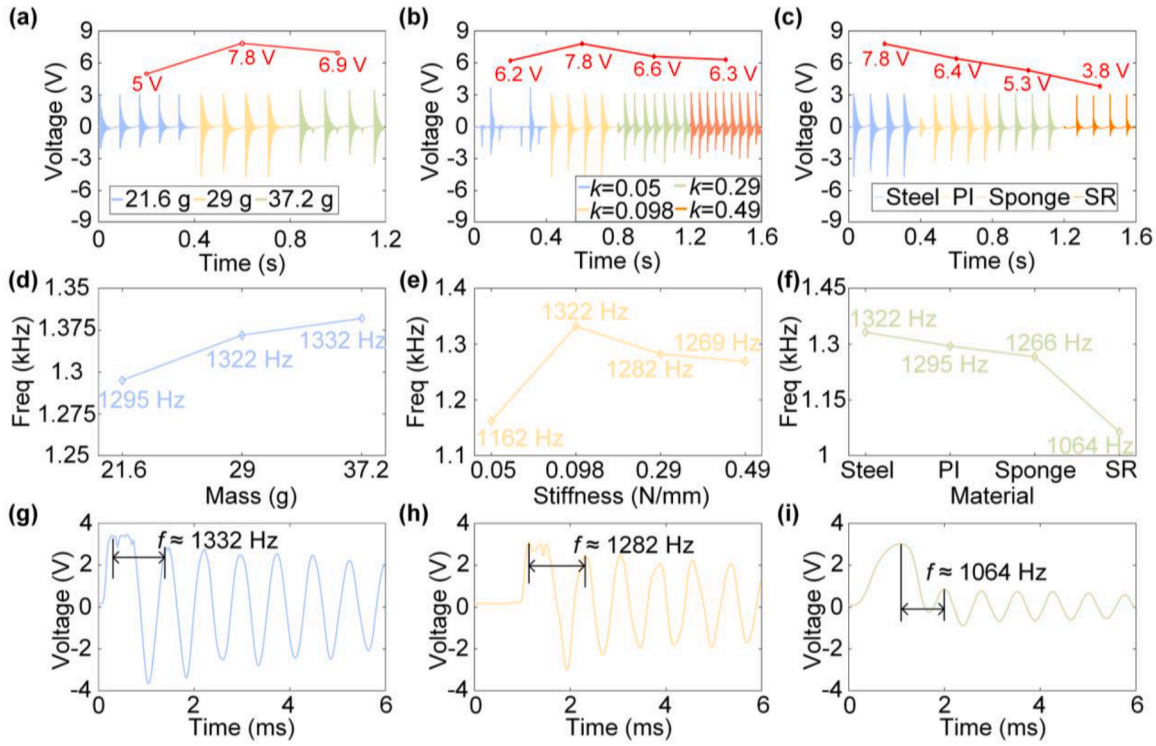

Fig. 9. Time-domain voltage response and instantaneous voltage outputs from different experiment conditions in resonant frequency regions under excitation acceleration of 0.75G: (a) Time-domain voltage response with k = 0.098 N/mm but different proof masses (21.6, 29, and 37.2 g) and no gasket; (b) Time-domain voltage response with m = 29 g but different spring stiffness (0.05, 0.098, 0.29, and 0.49 N/mm) and no gasket; (c) Time-domain voltage response with k = 0.098 N/mm and m = 29 g, but different material gaskets (PI, sponge, and SR); (d) the frequency of instantaneous voltage output with different proof mass (21.6, 29, and 37.2 g) and k = 0.098 N/mm without gaskets; (e) the frequency of instantaneous voltage output with different spring stiffness (0.05, 0.098, 0.29, and 0.49 N/mm) and m = 29 g without gaskets; (f) the frequency of instantaneous voltage output with different gasket materials (PI, sponge, and SR) and k = 0.098 N/mm and m = 29 g; (g) Instantaneous voltage output with proof mass of 37.2 g and spring stiffness of 0.098 N/mm, but no gasket; (h) Instantaneous voltage output with proof mass of 29 g and spring stiffness of 0.29 N/mm, but no gasket; (i) Instantaneous voltage output with m = 29 g, k = 0.098 N/mm, and an SR gasket.

Note that by using gaskets made of SR and PI materials, the bandwidths are significantly narrowed down. The retraction is because a softer material indicates a smaller impact stiffness and a weakened hardening effect. However, using the sponge gasket, the bandwidth is substantially enlarged. On the other hand, a softer material should lead to a smaller voltage amplitude due to a weakened amplitude truncation effect. However, sponge, SR, and PI materials may increase the damping and cause energy loss during the impact. Therefore, with gaskets made of sponge, SR, and PI materials, the voltage output from the 2DoF SPEH is decreased. Although using a steel gasket slightly increases the voltage output amplitude, considering the trade-off between the amplitude and the bandwidth, the sponge gasket is deemed the best choice to obtain the optimal 2DoF SPEH.

It is well known that the dynamic behaviour of a nonlinear system also depends on the excitation magnitude. We have conducted experiments under different excitation accelerations in one of our previously published articles [76]. It can be easily inferred that the 2DoF SPEH will exhibit stronger nonlinear behaviour and a more pronounced impact-induced amplitude truncation effect with increased acceleration. In general, a larger excitation magnitude always results in a larger voltage amplitude, since the amplitude truncation effect is reinforced. Therefore, a larger excitation acceleration is deemed more favourable from the perspectives of the broadband low-frequency energy harvesting and enhancing the output performance of the 2DoF SPEH.

To provide further insight into the dynamics of the 2DoF SPEH, steady-state time-domain responses picked from the resonant regions are demonstrated in Fig. 9, which were measured under a constant acceleration of 0.75 G. The excitation frequencies of the prototypes (k = 0.098 N/mm, no gasket) with proof masses of 21.6, 29, and 37.2 g are 21.6, 10.8, and 9.7 Hz, respectively. The excitation frequencies of the prototypes (m = 29 g, no gasket) with spring stiffnesses of 0.05, 0.098, 0.29, and 0.49 N/mm are 9.1, 10.8, 18.1, and 22.3 Hz, respectively. The excitation frequencies of the prototypes (k = 0.098 N/mm, m = 29 g) with PI, sponge, and SR gaskets were all set to 10.8 Hz.

Although the external excitation is of low frequency, the dynamic responses of the 2DoF SPEH contain high-frequency components due to the impact-induced frequency up-conversion mechanism. Regardless of the system parameters, the time-history voltage responses all behave similarly to pulse signals, as demonstrated in the subfigures in the first row of Fig. 9. The frequency up-conversion mechanism forms the pulse-like signals. The external excitation drives the 2DoF SPEH to "slowly" vibrate. Once impact occurs in the 2DoF SPEH, high-frequency oscillations are incurred. The frequency up-conversion effect can significantly increase the power density of the 2DoF SPEH. In Fig. 9(a), it is found that when the proof mass is 29 g, the voltage peak amplitude is the maximum amongst the three cases. By fixing the proof mass to be 29 g and varying the spring stiffness, the results in Fig. 9(b) indicate that k = 0.098 N/mm leads to the maximum voltage peak amplitude. As the spring stiffness decreases from 0.49 N/mm to 0.098 N/mm, the steady-state response voltage progressively increases, indicating that the impact-induced amplitude truncation effect is enhanced in the nonlinear system. The system is inclined to produce impact at lower spring stiffness, and if the spring stiffness surpasses a threshold, the impact is unlikely to occur. However, if the spring stiffness is too small ($\leq$0.05 N/mm), the spring cannot deliver sufficient spring force, resulting in weakened impact and decreased voltage. Given m = 29 g and k = 0.098 N/mm, Fig. 9(c) compares the effects of gaskets made of different materials. Note that with the decrease of the gasket material stiffness, the voltage peak amplitude decreases.

The second row of Fig. 9 reveals the resultant high-frequency

components after up-conversion for the systems with different proof masses, spring stiffness, and gasket materials. The last row of Fig. 9 presents the enlarged view of the time-history responses of the 2DoF SPEH over a single pulse period, from which the high-frequency component can be analysed. For instance, when the spring stiffness is 0.098 N/mm, and the proof mass is 37.2 g, under an external excitation of approximately 9.7 Hz, the response frequency of the 2DoF SPEH is increased to 1332 Hz, which means an increase of tens and even hundreds of times. As the response frequency is significantly increased, the power output density of the 2DoF SPEH is remarkably enhanced. It can be observed that the voltage response curve in Fig. 9(i) is smoother than those in Fig. 9(g) and (h). This is because the case associated with Fig. 9 (i) used an SR gasket, which is a relatively much softer material that can buffer the impact. In other words, SR material can increase the damping and energy loss during the impact. Therefore, the response curve of the highly-damped case is smoother. The concomitant consequence is that the voltage amplitude is drastically reduced.

4.3. Optimal power analysis

This section investigates the influence of the impact-induced amplitude truncation effect on the output power performance of the harvester. A series of experiments was carried out in the load spectrum to study the influence of different system parameters on the output power of the 2DoF SPEH, which is verified via capacitor charging tests. In addition to the voltage, another crucial parameter that indicates the performance of the harvester is the instantaneous power (P), which the following formula can calculate:

$$P = V_{p-p}^2 \Big/ R_m \tag{27}$$

in which $V_{p\text{-}p}$ and R_m are the peak-to-peak voltage across the external load and the resistance of the external load, respectively, since the harvester produces a pulse-like voltage output, the optimal resistance of the piezo-stack can be theoretically estimated by $R_m = 1/(2\pi f C_p)$[77], in which f and C_p represent the frequency of high-frequency oscillation and the capacitance of the piezo-stack, respectively. The optimal impedance is inversely proportional to the frequency. In the previous section, it was noted that the impact-induced frequency up-conversion can significantly magnify the frequency of the instantaneous voltage response. Therefore, it can be predicted that the optimal resistance of the harvester should decrease with the increase of the instantaneous voltage frequency. Fig. 10(a)–(d) presents the power output from the 2DoF SPEH measured in the experiment by varying the resistance. It is observed that the instantaneous power increases with the growth of the external load and reaches the maximum value when impedance-matching is achieved. The voltage monotonously increases with the external resistance until it approaches the open-circuit condition. From Fig. 10(a), it is noted that under excitation with the frequency of 10.8 Hz and the acceleration of 0.75 G, the maximum instantaneous peak power with the proof mass of 29 g is 521.6 mW when the spring stiffness of the harvester is tuned to k = 0.098 N/mm. Moreover, the estimated optimal resistance of the piezoelectric stack is 72.9 Ω, which is in agreement with the experimental result (i.e., 72.3 Ω). When the spring stiffness is tuned to k = 0.49 N/mm, the optimal resistance is estimated to be 72.6 Ω. The optimal resistance determined in the experiment is about 69.7 Ω (Fig. 10 (b)). Overall speaking, the experimental result is at the same level as predicted by the theory. When the sponge and SR gaskets are used, the corresponding optimal resistance is estimated to be 72.6 Ω and 86.4 Ω, respectively. The experimental results in Fig. 10(c) and (d) are basically consistent with the theoretical predictions. In addition to the instantaneous peak power, the root-mean-square (RMS) power (P_{rms}) of the energy harvester is investigated. The following formula can be used to calculate the RMS power of the 2DoF SPEH:

$$p_{rms} = \frac{\int_0^T U^2(t)/R_m dt}{T} \tag{28}$$

The results are presented in Fig. 10(e) and (f). From Fig. 10(e), it can be seen that when no gasket is used, the maximum RMS power of 8.75 mW is achieved by tuning the spring stiffness to 0.098 N/mm. When gaskets made of different materials are used, the RMS power decreases as the gasket material becomes softer (Fig. 10(f)). The RMS power of the case without using the gasket is 4.83 times as hugh as that of the case using an SR gasket. The up-conversion mechanism induced high frequency in the former case is 1.24 times as high as that in the latter. This finding indicates that a slight reduction in frequency leads to a significant decrease in the RMS power.

To demonstrate the energy harvesting ability of the harvester in a relatively real application, capacitor charging tests are conducted, and the effective power of the harvester is calculated. A 220 μF capacitor with a maximum voltage of 25 V is used in the test. In the first test, the excitation acceleration is controlled at 0.75 G; the proof mass is fixed at 29 g, and the spring stiffness is varied. The results are illustrated in Fig. 11(a).

The charging time is 5 s, and the final voltage varies with the spring stiffness. Obviously, a higher charging voltage within the same period means a better energy harvesting performance. The final charging voltages of the cases with spring stiffness of 0.05, 0.29, and 0.49 N/mm are 0.86, 1.8, and 1.53 V, respectively. The case with the spring stiffness tuned to 0.098 N/mm yields the maximum charging voltage (i.e., 2.23

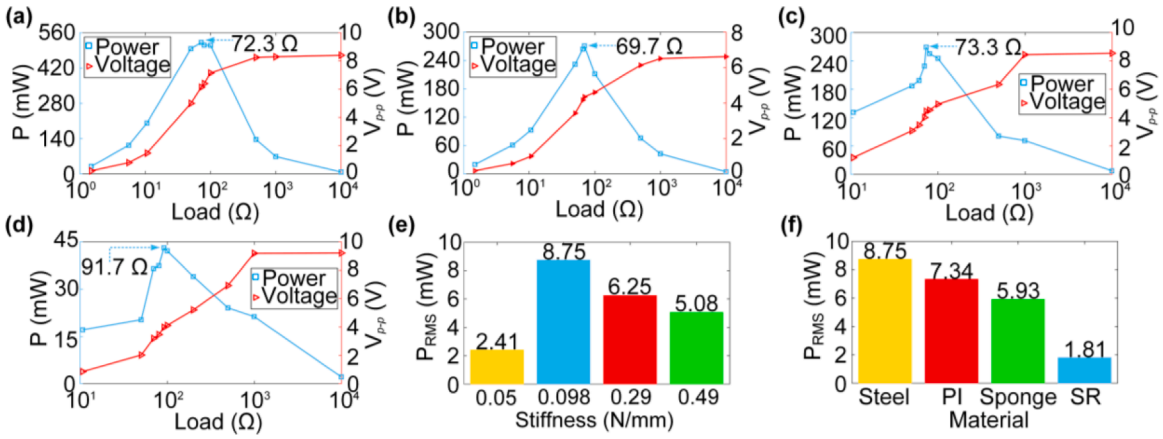

Fig. 10. The peak-peak voltage & instantaneous power and the RMS power from the 2DoF SPEH: (a) the power output and peak-peak voltage of k = 0.098 N/mm; (b) the power output and peak-peak voltage of k = 0.49 N/mm; (c) the power output and peak-peak voltage of sponge gasket;(d) the power output and peak-peak voltage of SR gasket; (e) the RMS power for different spring stiffness (0.05, 0.098, 0.29, and 0.49 N/mm);(f) the RMS power for different gasket material (PI, sponge, and SR).

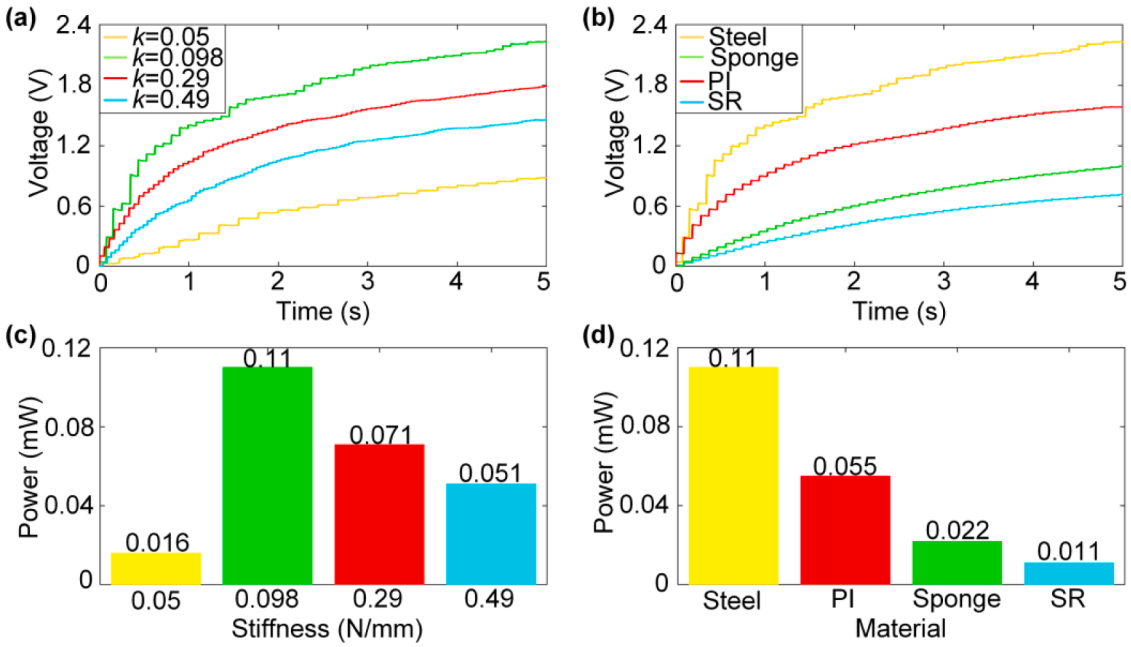

Fig. 11. Charging performance of the 2DoF SPEH using a 220 μF capacitor: (a) charging curves of the cases using different spring stiffness (0.05, 0.098, 0.29, and 0.49 N/mm); (b) charging curves of the cases using different gasket material (PI, sponge, and SR); (c) the average power of the cases using different spring stiffness; (d) the average power of the cases using different gasket materials.

V). This result agrees with the conclusion obtained from Fig. 10(a). In the second test, the spring stiffness is fixed to 0.098 N/mm, and gaskets of different materials are used. The voltage charging histories are shown in Fig. 11(b). As expected, when the gasket material becomes softer, the charging voltage decreases. The following formula can calculate the average charging power:

$$P = \frac{C\left(U_2^2 - U_1^2\right)}{2t} \tag{29}$$

in which P, C, U_1, U_2, and t are the average power, the capacitance of the capacitor used in the test, the initial voltage, the final voltage, and the charging time, respectively. In Fig. 11(c) and (d), the average power corresponding to those tests is plotted. For example, the average power of the condition with the spring stiffness tuned to 0.098 N/mm is 0.11 mW. When the spring stiffness is tuned to 0.49 N/mm, the power decreases to 0.051 mW. Fig. 11(c) clearly shows that the charging power decreases with the decrease of the impact stiffness (i.e., the gasket material becomes softer). In general, the excellent energy harvesting performance of the harvester due to the frequency up-conversion mechanism is validated.

5. Conclusions

In conclusion, this paper has proposed a 2DoF SPEH with excellent energy harvesting performance. The frequency up-conversion mechanism has been subtly employed to adapt a high-strength piezoelectric stack for low-frequency energy harvesting. The theoretical model of the 2DoF SPEH has been presented, and the approximated analytical solution was derived. An equivalent circuit model (ECM) has been established for capturing the dynamic characteristics of the 2DoF SPEH. The experimental results validated the theoretical and ECM models. A parametric study has revealed the effects of various system parameters (proof mass, spring stiffness, and impact stiffness) on the performance of the 2DoF SPEH.

The dynamic characteristics of the proposed 2DoF SPEH are summarized as follows. First, a suitable proof mass and a spring stiffness combination can yield a 2DoF SPEH with an enlarged bandwidth and enhanced instantaneous power peak. Second, increasing the impact stiffness can lead to a higher instantaneous power peak. However, considering the trade-off between the bandwidth and the power peak, a sponge gasket should be selected to soften the impact properly.

A comparative study has shown that when the proof mass is fixed at 29 g, and the spring stiffness of the harvester is tuned to 0.098 N/mm, the 2DoF SPEH can produce instantaneous power with a peak amplitude of 521.6 mW under an excitation of 10.8 Hz. The impedance-matching analysis demonstrates that the optimal resistance of the 2DoF SPEH is approximately 70 Ω.

CRediT authorship contribution statement

Zhongjie Li: Conceptualization, Methodology, Software, Formal analysis, Investigation, Visualization, Resources, Funding acquisition, Writing – original draft. **Xuzhang Peng:** Methodology, Software, Investigation, Visualization, Writing – original draft. **Guobiao Hu:** Methodology, Software, Formal analysis, Supervision, Writing – review & editing. **Yan Peng:** Resources, Supervision, Writing – review & editing.

Declaration of Competing Interest

The authors declare that they have no known competing financial interests or personal relationships that could have appeared to influence the work reported in this paper.

Acknowledgement

This work was supported in part by the National Natural Science Foundation of China (No.: 61773254; No.: 62001281) and the Shanghai Sailing Program (No.: 20YF1412700).

Supplementary materials

Supplementary material associated with this article can be found, in the online version, at doi:10.1016/j.ijmecsci.2022.107299.

References

[1] Li Z, Peng Y, Xu Z, Peng J, Xin L, Wang M, Luo J, Xie S, Pu H. Harnessing energy from suspension systems of oceanic vehicles with high-performance piezoelectric generators. Energy 2021;228.

[2] Wang M, Yin P, Li Z, Sun Y, Ding J, Luo J, Xie S, Peng Y, Pu H. Harnessing energy from spring suspension systems with a compressive-mode high-power-density piezoelectric transducer. Energy Convers Manag 2020;220.

[3] Zhou S, Zuo L. Nonlinear dynamic analysis of asymmetric tristable energy harvesters for enhanced energy harvesting. Commun Nonlinear Sci Numer Simul 2018;61:271–84.

[4] Sui G, Shan X, Tian H, Wang L, Xie T. Study on different underwater energy harvester arrays based on flow-induced vibration. Mech Syst Signal Process 2022;167.

[5] Tian H, Shan X, Sui G, Xie T. Enhanced performance of piezoaeroelastic energy harvester with rod-shaped attachments. Energy 2022;238.

[6] Peng Y, Zhang D, Luo J, Xie S, Pu H, Li Z. Power density improvement based on investigation of initial relative position in an electromagnetic energy harvester with self-powered applications. Smart Mater Struct 2021;30.

[7] Li Z, Liu Y, Yin P, Peng Y, Luo J, Xie S, Pu H. Constituting abrupt magnetic flux density change for power density improvement in electromagnetic energy harvesting. Int J Mech Sci 2021;198.

[8] Li Z, Jiang X, Yin P, Tang L, Wu H, Peng Y, Luo J, Xie S, Pu H, Wang D. Towards self-powered technique in underwater robots via a high-efficiency electromagnetic transducer with circularly abrupt magnetic flux density change. Appl Energy 2021;302:117569.

[9] Peng Y, Zhang L, Li Z, Luo J, Xie S, Pu H, et al. Experimental Investigation of Coil Thickness in Electromagnetic Energy Harvesters for Power Density Improvement. In: Jing X, Ding H, Wang J, editors. Conference Experimental Investigation of Coil Thickness in Electromagnetic Energy Harvesters for Power Density Improvement, Singapore. Singapore: Springer. p. 1078–1091.

[10] Miao G, Fang S, Wang S, Zhou S. A low-frequency rotational electromagnetic energy harvester using a magnetic plucking mechanism. Appl Energy 2022:305.

[11] Tao K, Lye SW, Miao J, Tang L, Hu X. Out-of-plane electret-based MEMS energy harvester with the combined nonlinear effect from electrostatic force and a mechanical elastic stopper. J Micromech Microeng 2015;25:104014.

[12] Ahmed S, Kakkar V. An electret-based angular electrostatic energy harvester for battery-less cardiac and neural implants. IEEE Access 2017;5:19631–43.

[13] Zhang Y, Wang T, Luo A, Hu Y, Li X, Wang F. Micro electrostatic energy harvester with both broad bandwidth and high normalized power density. Appl Energy 2018;212:362–71.

[14] Hu G, Zhao C, Yang Y, Li X, Liang J. Triboelectric energy harvesting using an origami-inspired structure. Appl Energy 2022;306:118037.

[15] Shen F, Li Z, Guo H, Yang Z, Wu H, Wang M, Luo J, Xie S, Peng Y, Pu H. Recent advances towards ocean energy harvesting and self-powered applications based on triboelectric nanogenerators. Adv Electron Mater 2021;7.

[16] Li Z, Saadatnia Z, Yang Z, Naguib H. A hybrid piezoelectric-triboelectric generator for low-frequency and broad-bandwidth energy harvesting. Energy Convers Manag 2018;174:188–97.

[17] Li Z, Luo J, Xie S, Xin L, Guo H, Pu H, Yin P, Xu Z, Zhang D, Peng Y, Yang Z, Naguib H. Instantaneous peak 2.1 W-level hybrid energy harvesting from human motions for self-charging battery-powered electronics. Nano Energy 2021;81.

[18] Li Z, Xin C, Peng Y, Wang M, Luo J, Xie S, et al. Power Density Improvement of Piezoelectric Energy Harvesters via a Novel Hybridization Scheme with Electromagnetic Transduction. Micromachines 2021;12(7):803.

[19] Hou C, Li C, Shan X, Yang C, Song R, Xie T. A broadband piezo-electromagnetic hybrid energy harvester under combined vortex-induced and base excitations. Mech Syst Signal Process 2022;171.

[20] Xu X, Wang Y, Li P, Xu W, Wei L, Wang Z, Yang Z. A leaf-mimic rain energy harvester by liquid-solid contact electrification and piezoelectricity. Nano Energy 2021;90.

[21] Tian H, Shan X, Cao H, Xie T. Enhanced performance of airfoil-based piezoaeroelastic energy harvester: numerical simulation and experimental verification. Mech Syst Signal Process, 162; 2022.

[22] Tian H, Shan X, Zhang J, Sui G, Xie T. Performance investigation of piezoaeroelastic energy harvester with trailing-edge flap. Sens Actuators A 2022;334.

[23] Shan X, Sui G, Tian H, Min Z, Feng J, Xie T. Numerical analysis and experiments of an underwater magnetic nonlinear energy harvester based on vortex-induced vibration. Energy 2022:241.

[24] Lu ZQ, Chen J, Ding H, Chen LQ. Two-span piezoelectric beam energy harvesting. Int J Mech Sci 2020;175.

[25] Zhang H, Sui W, Yang C, Zhang L, Song R, Wang J. An asymmetric magnetic-coupled bending-torsion piezoelectric energy harvester: modeling and experimental investigation. Smart Mater Struct 2021;31.

[26] Ray CA, Anton SR. Evaluation of piezoelectret foam in a multilayer stack configuration for low-level vibration energy harvesting applications. Active and Passive Smart Structures and Integrated Systems 2015;9431:328–38.

[27] Jiang X, Li Y, Li J, Wang J. Electromechanical modeling of a PZT disc-type energy harvester for large force vibration. Conference Electromechanical modeling of a PZT disc-type energy harvester for large forcevibration 2012:411–6.

[28] Li Z, Peng X, Hu G, Zhang D, Xu Z, Peng Y, Xie S. Towards real-time self-powered sensing with ample redundant charges by a piezostack-based frequency-converted generator from human motions. Energy Convers Manag 2022;258.

[29] Chen X, Li Y. Design, modeling and testing of a vibration absorption device with energy harvesting based on force amplifier and piezoelectric stack. Energy Convers Manag 2022;255.

[30] Kim H, Kim J, Wu H, Zhang B, Dayton PA, Jiang X. A multi-pillar piezoelectric stack transducer for nanodroplet mediated intravascular sonothrombolysis. Ultrasonics 2021;116.

[31] Qian F, Xu TB, Zuo L. Material equivalence, modeling and experimental validation of a piezoelectric boot energy harvester. Smart Mater Struct 2019;28:075018.

[32] Caetano VJ, Savi MA. Star-shaped piezoelectric mechanical energy harvesters for multidirectional sources. Int J Mech Sci 2022;215.

[33] Fang S, Chen K, Xing J, Zhou S, Liao WH. Tuned bistable nonlinear energy sink for simultaneously improved vibration suppression and energy harvesting. Int J Mech Sci 2021;212.

[34] Jia J, Shan X, Zhang X, Xie T, Yang Y. Equivalent circuit modeling and analysis of aerodynamic vortex-induced piezoelectric energy harvesting. Smart Mater Struct 2022;31.

[35] Xu TB, Siochi EJ, Kang JH, Zuo L, Zhou W, Tang X, Jiang X. Energy harvesting using a PZT ceramic multilayer stack. Smart Mater Struct 2013;22.

[36] Anton SR, Sodano HA. A review of power harvesting using piezoelectric materials (2003–2006). Smart Mater Struct 2007;16:R1–21.

[37] Wang C, Wang S, Li QJ, Wang X, Gao Z, Zhang L. Fabrication and performance of a power generation device based on stacked piezoelectric energy-harvesting units for pavements. Energy Convers Manag 2018;163:196–207.

[38] Jasim A, Yesner G, Wang H, Safari A, Maher A, Basily B. Laboratory testing and numerical simulation of piezoelectric energy harvester for roadway applications. Appl Energy 2018;224:438–47.

[39] Wang C, Song Z, Gao Z, Yu G, Wang S. Preparation and performance research of stacked piezoelectric energy-harvesting units for pavements. Energy Build 2019;183:581–91.

[40] Peng ZXY, Wang M, Li Z, Peng J, Luo J, Xie S, Pu H, Yang Z. Investigation of frequency-up conversion effect on the performance improvement of stack-based piezoelectric generators. Renew Energy 2021.

[41] Xu X, Cao D, Yang H, He M. Application of piezoelectric transducer in energy harvesting in pavement. Int J Pavement ResTechnol 2018;11:388–95.

[42] Wang C, Wang S, Gao Z, Wang X. Applicability evaluation of embedded piezoelectric energy harvester applied in pavement structures. Appl Energy 2019;251:113383.

[43] Song GJ, Cho JY, Kim KB, Ahn JH, Song Y, Hwang W, et al. Development of a pavement block piezoelectric energy harvester for self-powered walkway applications. Appl Energy 2019;256:113916.

[44] Cao DX, Duan XJ, Guo XY, Lai SK. Design and performance enhancement of a force-amplified piezoelectric stack energy harvester under pressure fluctuations in hydraulic pipeline systems. Sens Actuators A 2020;309:112031.

[45] Yang H, Wang L, Hou Y, Guo M, Ye Z, Tong X, et al. Development in stacked-array-type piezoelectric energy harvester in asphalt pavement. J Mater Civ Eng 2017;29:04017224.

[46] Moure A, Izquierdo Rodríguez MA, Rueda SH, Gonzalo A, Rubio-Marcos F, Cuadros DU, Pérez-Lepe A, Fernández JF. Feasible integration in asphalt of piezoelectric cymbals for vibration energy harvesting. Energy Convers Manag 2016;112:246–53.

[47] Zhang Y, Jin Y, Xu P. Dynamics of a coupled nonlinear energy harvester under colored noise and periodic excitations. Int J Mech Sci 2020;172.

[48] Gao Y, Liang J, Liao Y. Multiple harmonics extended impedance model of piezoelectric energy harvesting systems. IEEE/ASME Trans Mechatron 2021;27:1185–95. 1-1.

[49] Wang Y, Chen W, Guzman P, Zuo L. Amplified energy harvester from footsteps: design, modeling, and experimental analysis. Active and Passive Smart Structures and Integrated Systems 2014;9057:905724.

[50] Chen G, Tang L, Mace BR. Modelling and analysis of a thermoacoustic-piezoelectric energy harvester. Appl Therm Eng 2019;150:532–44.

[51] Qian F, Xu TB, Zuo L. Design, optimization, modeling and testing of a piezoelectric footwear energy harvester. Energy Convers Manag 2018;171:1352–64.

[52] Wang Y, Chen W, Guzman P. Piezoelectric stack energy harvesting with a force amplification frame: modeling and experiment. J Intell Mater Syst Struct 2016;27:2324–32.

[53] Ma X, Li H, Zhou S, Yang Z, Litak G. Characterizing nonlinear characteristics of asymmetric tristable energy harvesters. Mech Syst Signal Process 2022;168.

[54] Qian F, Xu TB, zuo L. A distributed parameter model for the piezoelectric stack harvester subjected to general periodic and random excitations. Eng Struct 2018;173:191–202.

[55] Chen S, Wang L, Zhou W, Musgrave P, Xu TB, Zuo L. Optimal design of force magnification frame of a piezoelectric stack energy harvester. Sensors and Smart Structures Technologies for Civil, Mechanicaland Aerospace Systems 2015;9435:386–96.

[56] Zhao S, Erturk A. Deterministic and band-limited stochastic energy harvesting from uniaxial excitation of a multilayer piezoelectric stack. Sens Actuators A 2014;214:58–65.

[57] Shevtsov S, Flek M. Random vibration energy harvesting by piezoelectric stack charging the battery. Procedia Eng 2016;144:645–52.

[58] Rezaei M, Talebitooti R, Liao WH. Exploiting bi-stable magneto-piezoelastic absorber for simultaneous energy harvesting and vibration mitigation. Int J Mech Sci 2021;207.

[59] Xu M, Li X. Stochastic averaging for bistable vibration energy harvesting system. Int J Mech Sci 2018;141:206–12.

[60] Dhote S, Yang Z, Behdinan K, Zu J. Enhanced broadband multi-mode compliant orthoplanar spring piezoelectric vibration energy harvester using magnetic force. Int J Mech Sci 2018;135:63–71.
[61] Rezaei M, Talebitooti R. Wideband PZT energy harvesting from the wake of a bluff body in varying flow speeds. Int J Mech Sci 2019;163.
[62] Staaf LGH, Smith AD, Lundgren P, Folkow PD, Enoksson P. Effective piezoelectric energy harvesting with bandwidth enhancement by assymetry augmented self-tuning of conjoined cantilevers. Int J Mech Sci 2019;150:1–11.
[63] Yin Z, Gao S, Jin L, Guo S, Wu Q, Li Z. A shoe-mounted frequency up-converted piezoelectric energy harvester. Sens Actuators A 2021;318.
[64] Pyo S, Kwon DS, Ko HJ, Eun Y, Kim J. Frequency up-conversion hybrid energy harvester combining piezoelectric and electromagnetic transduction mechanisms. International Journal of Precision Engineering and Manufacturing-Green Technology 2022;9(1):241–51.
[65] Chen W, Mo JL, Xiang ZY, Wang AY, Liu QA, Qian HH. A new concept of frequency-excitation-up conversion to improve the yield of linear piezoelectric generators. Sens Actuators A 2021;325.
[66] Shi G, Chen J, Peng Y, Shi M, Xia H, Wang X, Ye Y, Xia Y. A piezo-electromagnetic coupling multi-directional vibration energy harvester based on frequency up-conversion technique. Micromachines 2020;11 (Basel).
[67] Onsorynezhad S, Abedini A, Wang F. Parametric optimization of a frequency-up-conversion piezoelectric harvester via discontinuous analysis. J Vib Control 2020; 26:1241–52.
[68] Zhang J, Qin L. A tunable frequency up-conversion wideband piezoelectric vibration energy harvester for low-frequency variable environment using a novel impact- and rope-driven hybrid mechanism. Appl Energy 2019;240:26–34.
[69] Panthongsy P, Isarakorn D, Janphuang P, Hamamoto K. Fabrication and evaluation of energy harvesting floor using piezoelectric frequency up-converting mechanism. Sens Actuators A 2018;279:321–30.
[70] Gu L, Livermore C. Impact-driven, frequency up-converting coupled vibration energy harvesting device for low frequency operation. Smart Mater Struct 2011;20.
[71] Liu H, Lee C, Kobayashi T, Tay CJ, Quan C. Investigation of a MEMS piezoelectric energy harvester system with a frequency-widened-bandwidth mechanism introduced by mechanical stoppers. Smart Mater Struct 2012;21.
[72] Li Z, Yang Z, Naguib H, Zu J. Design and studies on a low-frequency truss-based compressive-mode piezoelectric energy harvester. IEEE/ASME Trans Mechatron 2018;23:2849–58.
[73] Halim MA, Park JY. Theoretical modeling and analysis of mechanical impact driven and frequency up-converted piezoelectric energy harvester for low-frequency and wide-bandwidth operation. Sens Actuators A 2014;208:56–65.
[74] Tang L, Zhao L, Yang Y, Lefeuvre E. Equivalent circuit representation and analysis of galloping-based wind energy harvesting. IEEE ASME Trans Mechatron 2014;20: 834–44.
[75] Wang J, Tang L, Zhao L, Hu G, Song R, Xu K. Equivalent circuit representation of a vortex-induced vibration-based energy harvester using a semi-empirical lumped parameter approach. Int J Energy Res 2020;44:4516–28.
[76] Peng Y, Xu Z, Wang M, Li Z, Peng J, Luo J, Xie S, Pu H, Yang Z. Investigation of frequency-up conversion effect on the performance improvement of stack-based piezoelectric generators. Renew Energy 2021;172:551–63.
[77] Kim H, Priya S, Stephanou H, Uchino K. Consideration of Impedance Matching Techniques for Efficient Piezoelectric Energy Harvesting. IEEE Transactions on Ultrasonics, Ferroelectrics, and Frequency Control 2007;54(9):1851–9.